Particle-turbulence interaction of high Stokes number irregular shape particles in accelerating flow: a rocket-engine model

Sabrina Kalenko[a], Alexander Liberzon[a]

[a]Turbulence Structure Laboratory, School of Mechanical Engineering, Tel Aviv University, Tel Aviv 69978, Israel

ABSTRACT

The addition of metal particles to solid propellant rocket engines enhances combustion and engine performance. The particle-turbulence interaction mechanisms of the metal particles, or aggregates of particles, with the high Reynolds number turbulent gas flow, accelerating towards an engine nozzle, are not characterized thoroughly. We study experimentally the interactions of high Stokes number particles with high speed incompressible turbulent air flow in a simplified quasi-two-dimensional model of a rocket engine chamber. Two-phase particle image/tracking velocimetry (PIV/PTV) methods are combined to measure the turbulent air flow simultaneously with velocities of large Stokes/particle Reynolds number irregularly shaped inertial particles ($St \sim 70$, $Re_p \sim 300$). Comparing the turbulent fluctuations in the single phase flow (unladen case) to those in the two-phase flow, (particle-laden cases) we reveal the local augmentation of turbulent fluctuations in the wake regions of the inertial particles. Even at low mass fraction, the high Stokes number and slow response times lead to the global augmentation of turbulent kinetic energy (TKE). The particle response time scale is longer than all relevant flow time scales and longer than the particle residence time scale. This situation leads to a peculiar type of interaction that enhances turbulent kinetic energy everywhere in the flow attributable to efficient injection of turbulent kinetic energy caused by the the vortex shedding mechanism, followed by the mean flow transport. The increase of particle mass fraction towards the nozzle due to mass conservation and converging streamlines compensates for the dampening effect of the mean flow acceleration, and augments TKE before the flow passes the nozzle throat. Furthermore, this effect is accompanied by an unexpected isotropic turbulence in the proximity of the nozzle, different from the generally anisotropic accelerating flow in the chamber. The phenomena of the locally isotropic and highly enhanced turbulence in the proximity of the engine nozzle attributable to the low mass fraction, but high St, Re_p particles, is expected to improve design of solid propellant rocket engines. The experimental dataset can serve as a benchmark for the multi-phase simulations.

Keywords: Particle laden turbulent flow, Rocket engine, Turbulence modulation, Spatial acceleration

1. Introduction

Despite a vast body of research on the dynamics of dispersed particles in turbulence, we cannot predict whether TKE will be augmented or attenuated in complex flow cases (Balachndar and Eaton, 2010). For instance, apparently similar flow cases were reported to have contradicting trends in studies of particle-turbulence interaction in fully developed channel flows for different sizes and densities of particles Kulick, Fessler and Eaton (1994); Kussin and Sommerfeld (2002); Kiger and Pan (2002); Li, Wang, Li, Chen and Zheng (2012). Kulick et al. (1994) investigated turbulent flow in a vertical channel and found turbulence attenuation that increased with mass loading and Stokes number. Kiger and Pan (2002) showed turbulence augmentation far from the wall and negligible effect near the wall. Kussin and Sommerfeld (2002) found significant turbulence augmentation near the channel center plane for particles larger than η with particle Reynolds numbers above 350, and turbulence attenuation near the wall. Conversely, Li et al. (2012) found increased fluctuations near the wall and reduced fluctuations at the outer region of the boundary layer. Cisse, Homann and Bec (2013) developed a fully resolved direct numerical simulation around a relatively large particle at moderate particle Reynolds numbers, and using conditional analysis in the coordinate system relative to the particle position, have shown that particles reduce fluctuations in their wake. The authors presented particle fluid coupling at distances of one particle diameter and that particle essentially creates a "shadow in its wake". At larger particle Reynolds numbers, Hetsroni (1989) found augmentation of TKE. The authors explained this by the vortex shedding

*corr. author email: sabrinakalenko@gmail.com
ORCID(s):

mechanism in the wake of the particle. These examples are by no means a comprehensive review of existing literature. It is a small sample emphasizing that insignificantly different parameters, along with the carrier phase flow and particle properties, can produce substantially different effects of particles on the TKE.

Particle-fluid flow interaction is characterized by the ratios of a) length scales, namely the size of the particle relative to the relevant flow length scale, b) time scales, i.e. particle response time relative to the relevant flow time scale, or the Stokes number, c) particle Reynolds number, Re_p, based on the relative (sometimes called slip) velocity (Hetsroni, 1989; Tanaka and Eaton, 2008):

$$Re_p = \frac{|\boldsymbol{U} - \boldsymbol{V}_p| d_p}{\nu}, \tag{1}$$

where d_p is the particle diameter, $\boldsymbol{V}_p$ is the particle velocity (bold symbols denote vectors), ν is the fluid kinematic viscosity, and $\boldsymbol{U}$ is a so-called "undisturbed fluid velocity at the position of the particle", which is practically estimated as an interpolation of the surrounding fluid velocity to the position of the particle (e.g. Meller and Liberzon, 2015). The particle relaxation time τ_p for small and relatively heavy particles, $\rho_p \gg \rho_f$ and $Re_p < 1$ is defined as:

$$\tau_p = \frac{\rho_p d_p^2}{18\mu} \tag{2}$$

However, for higher Re_p a non-linear drag force correction is required (Crowe, Schwarzkopf, Sommerfeld and Tsuji, 2011):

$$\tau_p = \frac{\tau_p}{1 + 0.15\, Re_p^{0.687}} \tag{3}$$

The Stokes number is the time scales ratio (Crowe et al., 2011):

$$St = \frac{\tau_p}{\tau_f}. \tag{4}$$

Large Stokes number $St \gg 1$ means that particles response time is longer than the flow time scale. In this work the particles are larger than the Kolmogorov length scale ($d_p > \eta$), and heavier than the surrounding fluid ($\rho_p \gg \rho_f$). Therefore an appropriate flow time scale is that of the mean flow, i.e. $\tau_f = L/U$, where L is an turbulent integral scale.

The length scales ratio, d_p/L, where L is the integral length scale of turbulence, was proposed by Gore and Crowe (1989) to distinguish between attenuation for $d_p/L < 0.1$ and augmentation for $d_p/L > 0.1$.

Separately, aforementioned ratios of time/length scales could not predict reliably the augmentation/attenuation effect for different flow cases. Tanaka and Eaton (2008) suggested another dimensionless parameter that combines the Stokes number with the flow Reynolds number $Re_L = U L/\nu$ and turbulence scale separation η/L:

$$Pa = St\, Re_L^2\, (\eta/L)^3 \tag{5}$$

The authors (Tanaka and Eaton, 2008) combined empirical data from 80 experiments and demonstrated that in the range $10^3 < Pa < 10^5$ there is attenuation of TKE, while for all other cases (below 10^3 or above 10^5) there is an increase in TKE due to particles.

Gany, Caveny and Summerfield (1978) photographed aluminized solid propellants under crossflow conditions forming and burning in the form of agglomerates of Al/Al_2O_3. The primary particles of the order of 10 μm behaved like flow tracers and did not exhibit two-way coupling. However, the irregularly shaped agglomerates, in the range of 40 to 800 μm, that formed primarily on the surface during burning process, afterwards were detached and carried by the turbulent flow. Caveny and Gany (1979) studied breakup of agglomerates in aluminized propellants when the agglomerates burn slowly compared to residence time in the rocket motor. They found that the agglomerates velocity lags in the nozzle cause breakup of sufficiently large agglomerates and thereby permit reasonable combustion efficiencies to be achieved. The motion of large irregular particles resembling the agglomerates in the turbulent flow and their contribution to the TKE balance (augmentation vs attenuation) is the central question of this study.

In this work we study experimentally the effect of large, heavy and irregularly shaped particles on the TKE in a simplified model of a rocket engine. We reproduce the key features of the mean flow: a) acceleration towards the

nozzle; b) geometrical shape similarity of a contracting flow through a small nozzle throat; and c) particle sizes that correspond to metal agglomerates reported in the literature. In this flow there are competing effects of acceleration, particle-turbulence interaction, and monotonically increasing local mass fraction due to the contracting flow through the nozzle. To what extent various mechanisms contribute to the overall increase or decrease of turbulent kinetic energy is not yet clear.

This two-phase flow case is somewhat different from the aforementioned ones also, in the sense that the particle residence time in the flow is rather short as compared to the particle response time. Due to fluid acceleration towards the nozzle, all the key parameters, the relative velocity, Stokes number, particle Reynolds number, the fluid Reynolds number, all vary in the Lagrangian sense, or inhomogeneous in the Eulerian sense. The case is to some extent analogous to the interaction of large Stokes particles with the near to far-field of the jets Prevost, Boree, Nuglisch and Charnay (1996), but all the changes occur at the time scales shorter than the particle residence or response time.

We used particle image/tracking velocimetry (PIV/PTV) to measure simultaneously velocities of the fluid and particulate phases in two dimensions. In the most general case, a two-wavelength illumination and imaging would be necessary to distinguish between two phases Elhimer, Praud, Marchal, Cazin and Bazile (2017); Poelma, Westerweel and Ooms (2006). However, in this case the particles are much larger as compared to the flow tracers, and a simple PIV system is sufficient to separate particles and fluid tracers Khalitov and Longmire (2002); Hwang and Eaton (2006). Simultaneous measurements allow to estimate instantaneous slip velocity using local flow interpolation and to measure TKE, as well as its change in respect to the location of particles.

This manuscript is organized as follows. The experimental setup and methods are presented in Section 2, the results are reported in Section 3, followed by discussion and conclusions summarized in Section 4.

2. Experimental details

We created a quasi-two-dimensional experimental chamber (500 mm long, 245 mm wide and 35 mm front-to-back wall distance, nozzle throat width is 35 mm) which resembles a cross-section of a generic solid-propellant rocket motor with round symmetrical cavities (Volkov, Emel'yanov and Kurovs, 2012; Ciucci and Iaccarino, 2012), shown in Fig. 1. The back and front walls of the channel were made from glass and the side walls have optical windows to enable optical access for the laser sheet and particle imaging. The purpose is to create a quasi-two-dimensional velocity field as a proxy of the two-dimensional axisymmetric flow field in a cylindrically shaped rocket engine.

The chamber was positioned vertically with the main flow direction and the particle motion aligned with gravitational acceleration. The air was supplied by a blower through a converging channel (750 mm above the measurement region). The measurement volume is 140×105 mm, the lowest edge is 40 mm above the nozzle entrance, as shown in Fig. 1. Above this measurement location the flow resembles the fully developed channel flow, with constant streamwise velocity. Within the measurement, the region flow is spatially changing in both streamwise and spanwise directions, accelerating and converging into the nozzle. as shown in Fig. 1b.

Olive oil aerosol (1 μm droplets) produced by a Laskin nozzle seeder, and alumina particles supplied by a custom-made particle seeder, (both manufactured by I.T.E.S Engineering LLC, Israel) were mixed into the air stream before entering the chamber.

We measured turbulent flow and particle motion for two flow rates (low/high). The Reynolds number at the throat is based on the characteristic velocity defined by the volumetric flow rate through the chamber and the cross-sectional area of the nozzle. The Reynolds number at the throat is $Re_L = 185,000$ and $260,000$, for the low and high flow rates respectively. In our setup, L_t is the size of the nozzle throat, and the smallest dimension of the chamber determines the integral scale of the turbulent flow. Additional relevant parameters for the two experiments are given in Table 1.

The PIV setup consists of the double-head pulsed Nd:YAG laser (120 mJ/pulse, 532 nm, 15 Hz, New Wave Solo), with laser optics creating a light sheet with approximately 1 mm wide, and a 2672×4008 pixels double exposure 12 bit CCD camera (TSI Inc. Shoreview, MN), equipped with a 100 mm Nikon macro-lens at f/2.8 resulting in a spatial resolution of 42 μm/pixel.

For the PIV analysis we used Insight 3G software (TSI Inc.) and compared it to the open source software (Python version of OpenPIV). We used a multi-pass algorithm from 64×64 to 32×32 pixel interrogation windows, with 50% overlap. The multi-pass method increases the dynamic range which is especially important for the particle-laden flow cases, due to the high relative (slip) velocity. At each iteration, outliers vectors were rejected and replaced by the mean of the five nearest neighbors. The experiments consist of 4 runs at two flow rates with/without particles. Every experimental run consists of 5 sets (repetitions), 125 pairs of images each.

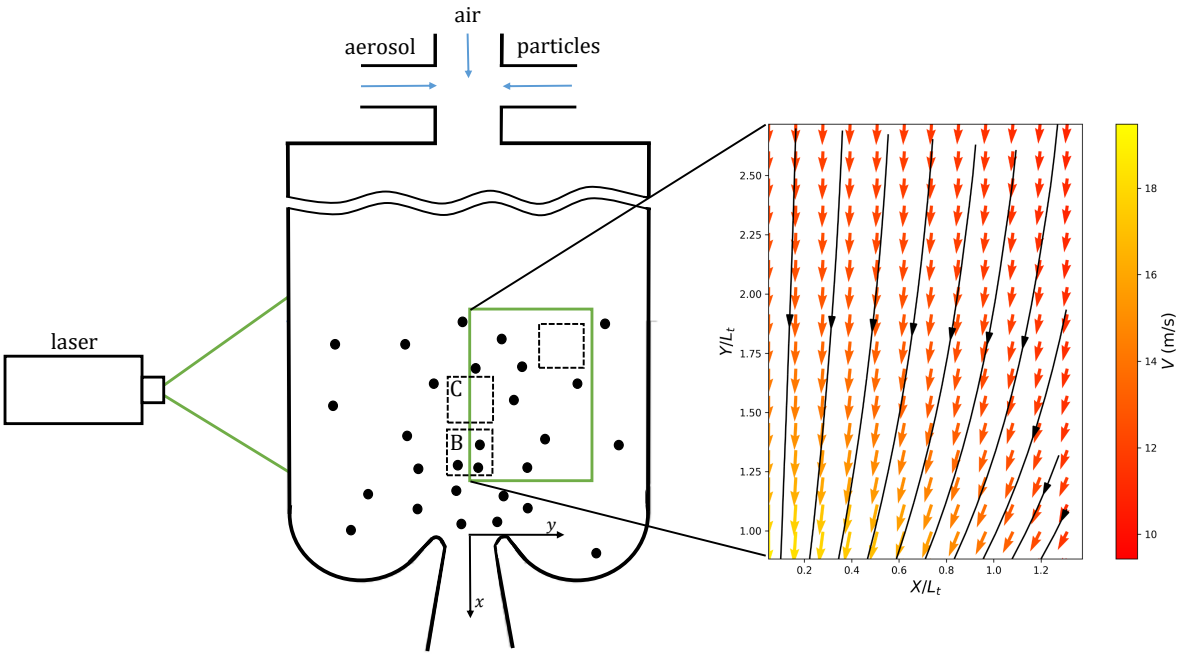

Figure 1: a) Schematic side view diagram of rocket engine model and PIV setup and picture of the experimental setup. The coordinate system is defined with x in the direction of the mean flow through the nozzle and y is the transverse direction, the origin is at the nozzle throat. b) Ensemble average velocity field and streamlines in the measurement region of 140 × 150 mm.

The mean flow in the region of interest is shown qualitatively in Fig. 1b as color-coded arrows and streamlines. Spatial coordinates x and y are normalized by the nozzle width L_t. Note that the position of the region of interest is shown in Fig. 1a. The bottom side is one nozzle throat length away from the nozzle entrance. The flow in the field of view is presented as a vector plot in Fig. 1b. The streamlines of the flow field for both Reynolds numbers are practically identical, except for the representative velocity scale at the nozzle throat of 96 m/s for the low flow rate, and 135 m/s for the high flow rate experiments.

2.1. Particles

We used non-spherical alumina particles that are common in solid propellant rocket engines and other industrial applications. An effective particle diameter d_p was measured with a Laser diffraction device (Malvern Analytical) and presented in Fig. 2a. In Fig. 2b we present the reciprocal of inscribed circle sphericity of the particles (Wadell, 1935; Riley, 1941), the square root of the ratio of the inscribed and circumscribed circles of the particle. The mean sphericity of 56 particles, examined under a microscope, is $\Psi = 0.81 \pm 0.1$. The microscopic images are shown in Fig. 2c emphasizing random shapes, sharp edges, rough surfaces, cavities, and protrusions.

In table 1 we present flow and particle parameters (some are given as the range of values in the chamber) for the two experiments. Using PIV data and aforementioned definitions in Eqs. (2), (4), we estimated the particle response time scales and the Stokes number. The residence times of the particles, estimated from $\tau_r = H/V_p$ when H is the height of the chamber and V_p in the mean particle velocity, were 30 to 40 ms. The ratio of particle response time, τ_p, to this residence time, τ_r, is between 2 to 4, for the two Reynolds number runs. This ratio explains that particles leave the chamber before they can respond to the air streamwise velocity.

Furthermore, we estimate the response of the particles to the spatial acceleration of streamwise velocity using the acceleration time scale, τ_a:

$$\tau_a = \left(dU_c/dx\right)^{-1} \tag{6}$$

that provides a similar ratio of scales, τ_a/τ_p. Mean slip due to acceleration of the flow is expected when $\tau_a/\tau_p > 1$.

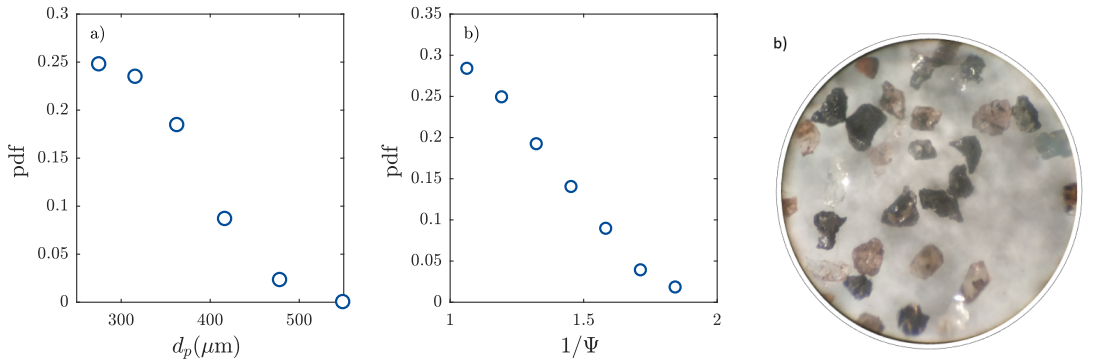

Figure 2: a) Probability density function (PDF) of particle effective diameters d_p, defined as a diameter of an equivalent sphere; b) PDF of reciprocal of sphericity Ψ^{-1} c) alumina particle's picture under a microscope.

Table 1
Particle and flow parameters: Re_L based on flow rate, τ_p is the particle response time, Eq (3), τ_a is the flow acceleration time scale, Eq. (6), τ_r is the particle residence time estimated from $\tau_r = H/V_p$ when H is the height of the chamber, t_f is the integral time scale $t_f = L_t/U_f$, St is the Stokes number, Eq. (4), τ_a is the acceleration time scale, Eq. (6), and particle Reynolds number, Eq. (1).

Exp.	Re_L	τ_p (ms)	τ_a (ms)	τ_r (ms)	t_f(ms)	S_t	τ_p/τ_r	τ_a/τ_p	Re_p
1	260000	75-90	0.1-1	30	9-11	85	2-3	0.0013- 0.011	300-450
2	185000	95-121	0.2-3.4	40	13-15	75	2-4	0.0021-0.028	450-650

In our flow, however, $\tau_a/\tau_p \ll 1$ is everywhere in the chamber (table 1). Thus these particles can be characterized in general as "unresponsive" (Hardalupas, Taylor and Whitelaw, 1989).

The time scale ratios do not mean that there is no particle-turbulence interaction or there is a weak interaction. Conversely, there is a substantial transfer of momentum between the particulate phase and the turbulent fluctuations of carrier flow, as will be explained in the following.

2.2. Two-phase PIV/PTV velocity analysis

We follow the procedure previously reported by Khalitov and Longmire (2002) among others. We filter PIV images, based on size and intensity of objects, (above 15 pixels in diameter and intensity level of 200/255) to create particle-free PIV images from which we obtain turbulent velocity fields. The separated images of large particles processed with particle tracking velocimetry (PTV) analysis, using the nearest neighbor algorithm is written in Matlab (Mathworks Inc.). In Fig. 3 we present an example of an instantaneous flow field (green arrows overlaying the original image) of the carrier phase and particulate phase on the left panel, and the fluctuating flow field (after subtracting the ensemble averaged flow field), shown in Fig. 1b.

3. Results

3.1. Local mass loading ratio, $\langle\phi\rangle$

The mass fraction or mass loading ratio, ϕ, is defined as the ratio of particle mass in respect to that of the fluid. We estimate local mass loading at various distances from the nozzle based on the number of particles, N, extracted from PIV images, and their size distribution, shown in Fig. 2a. The mass of particles are divided by the total mass of air. The volume of air is calculated as the area of interest in the PIV image, times the laser sheet thickness, excluding the volume of particles within the field of view.

The local mass loading, averaged for the ensemble of PIV images and horizontally across the measured region, $\langle\phi\rangle$, is presented in Fig. 4a. The flow is from right to left (from large x/L_t to low x/L_t the nozzle is at $x = 0$) and the mass loading increases as the flow/particles approach the nozzle. The mass loading was higher for lower flow rate and it increases at a steeper rate as the flow accelerates towards the nozzle. We will address this effect in the discussion.

The corresponding volume fractions are $\langle\phi_v\rangle = 4 \div 9 \times 10^{-4}$ for the low flow rate and $\langle\phi_v\rangle = 3 \div 4 \times 10^{-4}$ for the

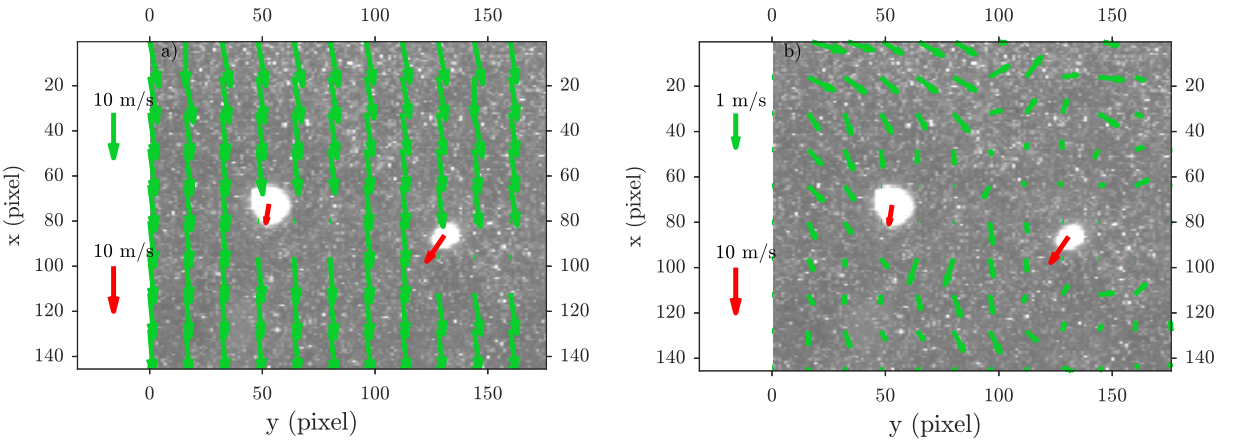

Figure 3: Instantaneous flow field of the carrier phase in the green vectors and particulate phase in the red vectors; a) for instantaneous flow field; and b) for the fluctuations, overlapped on the original PIV image. The flow field was taken from the dashed square in Fig. 1.

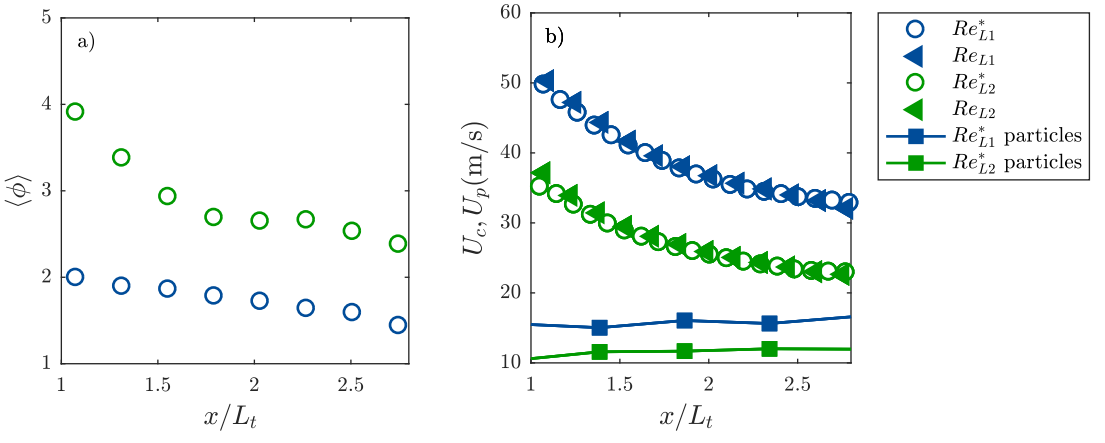

Figure 4: a) Averaged mass loading $\langle\phi\rangle$ as a function of distance from the nozzle; b) Air and particles average streamwise velocities versus the distance from the nozzle, along the centerline, $y = 0$.

high flow rate, respectively. The volume loading range corresponds to the two-way coupling regime, (Elghobashi and Trusedell, 1993), far from the four-way coupling regime $\langle\phi_v\rangle > 10^{-2}$, so particle-particle interaction can be safely neglected.

It should be noted that due to the two round cavities on both sides of the chamber from which particles rebound at high speed, few particles arriving at an angle to the flow field within the field of view were excluded from the present data.

3.2. Mean velocity

In Fig. 4b, we plot the average streamwise U velocity (capital letters hereinafter used for ensemble averaged quantities, lower case letters for fluctuating or turbulent quantities) for the particle unladen and laden cases (filled and open symbols, respectively) for the two Reynolds numbers (circles and triangles). In addition, we plot the average velocity of particles (squares and solid lines). Fig. 4b presents the values as a function of distance from the nozzle throat. We can summarize the key flow features visible in Fig. 4:

- horizontally averaged mass fraction and the mean streamwise velocity increase towards the nozzle ($\partial U/\partial x \approx$

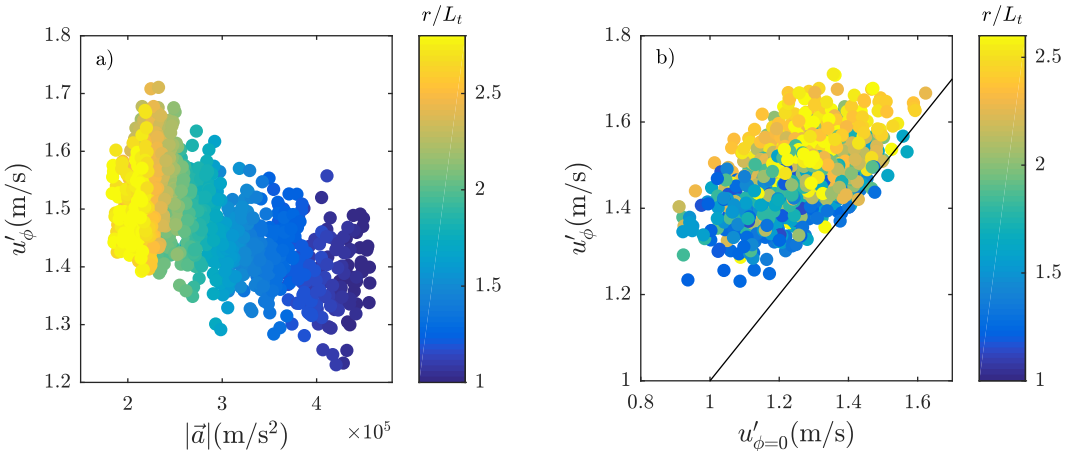

Figure 5: a) Scatter of r.m.s. of streamwise velocity fluctuations u' versus the flow spatial magnitude of acceleration $|\vec{a}|$, for Re_{L1}; b) Scatter of r.m.s. of velocity fluctuations for the particle laden case u'_ϕ versus the unladen case values $u'_{\phi=0}$, for Re_{L1}. In both plots the color-bar refers to the distance from the nozzle entrance r/L_t.

$(2 \div 10) \times 10^3$ s^{-1}) ;

- flow accelerates also from the sides of the chamber towards the centerline, with $\partial U/\partial y \approx (0.5 \div 3) \times 10^3$ s^{-1};
- average particle velocities, $\boldsymbol{V}_p$ are practically constant during the time particles cross the measurement volume;
- the average air velocity distribution and amplitude have not changed in particle-laden cases as compared to the unladen ones;
- the high Stokes/Reynolds number inertial particles move slower that the air flow, and preserve their velocity, as shown in Fig. 4b.

The particles ($\tau_p \approx 75 - 121$ ms, residence time in the chamber ≤ 40 ms) do not have enough time to respond to spatial streamwise velocity gradient, despite a strongly accelerating flow. This result is in agreement with the experiments of Gilbert, Davis and Altman (1955) and Gany et al. (1978); Caveny and Gany (1979), where agglomerates of $200 \div 1000$ μm were found to move slower as compared to the carrier flow everywhere in a two dimensional rocket motor chamber.

3.3. Turbulence and particle-turbulence interactions

Firstly, the mean flow acceleration towards the nozzle dampens turbulent fluctuations, as shown in Fig. 5a. We present the root-mean-square (r.m.s., $u' = \langle u^2 \rangle^{1/2}$) of velocity fluctuations, for the particle-laden case, versus the magnitude of flow acceleration (taking into account both streamwise and spanwise components). In addition to the scatter distribution of the values showing negative correlation between the acceleration and fluctuations, we add a color scale to emphasize the spatial distribution of the results. Thus, the color scale in 5a corresponds to the absolute distance from the nozzle entrance, r/L_t, where $r = \left(x^2 + y^2\right)^{1/2}$. As was shown above in Fig. 4b, the acceleration is stronger closer to the nozzle and this region is characterized by the lower turbulent fluctuations. The results are similar for both Reynolds numbers, as well as for laden and unladen cases, as shown in more details below.

Secondly, inertial particles in this flow augment fluctuations mainly in the streamwise component (and at a similar rate for both Reynolds numbers). Since the mean flow has not changed in the particle-laden cases (Fig. 4b), we can compare pointwise the root-mean-square of the streamwise flow fluctuations of the laden case u'_ϕ with the unladen case $u'_{\phi=0}$. This comparison is shown in Fig. 5b. Every scatter point in this figure above the straight line with a unity slope demonstrates the increased fluctuations in the particle-laden case. At some locations, the increase is up to 50% and it varies also with the spatial location. It is noteworthy that the turbulent fluctuations increased in the regions of different local mass fraction (compare the color change with the Fig. 4a).

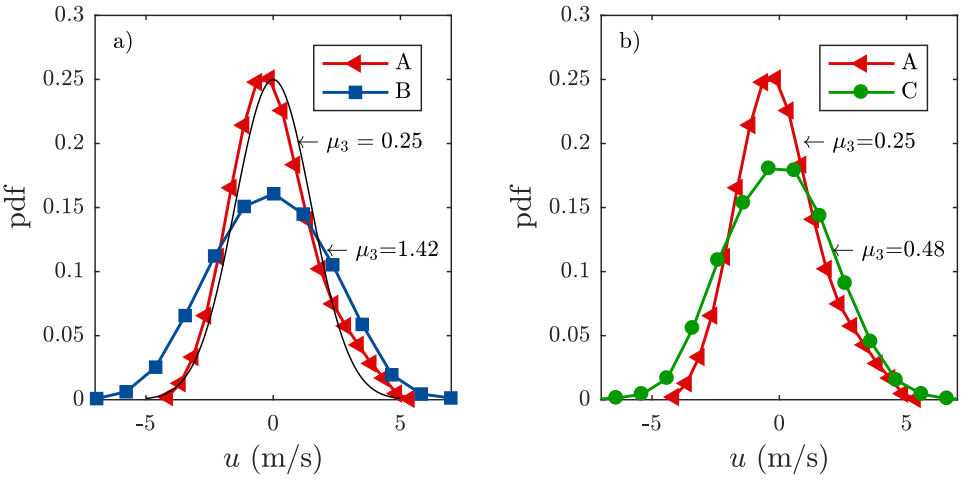

Figure 6: a) and b) PDF of streamwise velocity fluctuations at $x/L_t \approx 1.8$ at the centerline $y = 0$, where the red triangles denote the unladen case (A), blue squares denote the particle-laden flow with local accumulation of particles (B) and the green circles denote the particle-laden flow with locally clear air (C). Experimental values of skewness, μ are added to the respective PDFs and a thin black line of a Gaussian shape ($\mu_3 = 0$) is added for the reference.

Furthermore, we use conditional sampling to understand better the local and global effects of particles on the TKE. We divide the instantaneous PIV/PTV fields along the centerline into small control volumes of 20 × 20 mm, and conditionally sample the turbulent fluctuations depending on whether they contain particles, marked as regions B/C in Fig. 1a. Case B marks regions that contain at least one particle, while case C marks regions that do not contain inertial particles in the particle-laden runs.

In Figs. 6a,b we present a comparison of the probability distribution functions (PDF) of the streamwise fluctuations in the case of a unladen flow case (red triangles) with these at two conditional samples: the regions with at least one particle (B) (6a), and the regions in the particle-laden case that do not contain inertial particles (C). Both PDFs of the particle-laden cases have wider tails and exhibit higher u' values. In addition, the particle laden PDFs are skewed towards negative fluctuations. Skewness values, μ_3, are added to Fig. 6a,b (these are 0.25, 1.42 and 0.48 for cases A, B and C, respectively). Clearly the turbulent flow in the proximity of the particles is significantly different from the other flow regions, but the entire flow is "contaminated" by the negative velocity fluctuations, stemming from the local particle-turbulence interactions. Reflecting on the introductory section, we can attribute these local effects with negative fluctuations to the "vortex shedding" regime and infer that the wakes are transported and affect the flow for a substantially longer time scale as compared to the particle residence time.

In Fig. 7a, we add a quantitative measure of the differences shown in PDFs along the centerline as a function of distance from the nozzle. We also present the values of the u' and v' of the local/non-local conditional samples and of the unladen case together in order to emphasize the different rate of decrease of the fluctuations in the direction of mean flow acceleration. The ratio of r.m.s. of the fluctuations v'/u' which is in some sense a measure of anisotropy (a horizontal line at 1 means isotropic fluctuations) is shown in Fig. 7b.

We reveal very peculiar phenomena due to competition between the several effects: a) streamwise fluctuations strongly decrease towards the nozzle due to the mean flow acceleration; b) spanwise fluctuations increase towards the nozzle as the flow that converges from the sides has a lower momentum as compared to the accelerated flow at the centerline; c) particles increase fluctuations locally and globally, thus compensate the decrease due to acceleration; d) most surprisingly, because the effects a)-c) counteract each other, the wakes of the irregularly shaped particles created in the vortex shedding regime are isotropic unlike rest of the flow. The rates of change have similar trends and are linked to the local mass fraction, shown above in Fig. 4a.

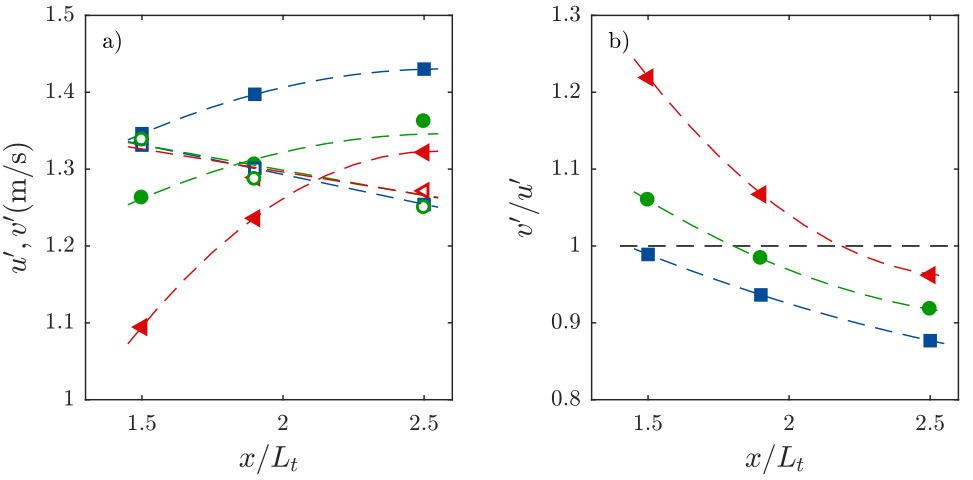

Figure 7: a)Root-mean-square of fluctuation components, v' and u', versus the distance to the nozzle x/L_t (same legend as in Fig. 6). Filled markers denote u' and open markers are for v'. b) anisotropy measure, v'/u' for the three cases A-C, a horizontal line at $v'/u' = 1$ emphasizes the isotropic ratio.

4. Summary and conclusions

In this work, we created the experimental setup of a two dimensional model of a rocket engine and studied the particle-turbulence interaction when the particulate phase consists of dispersed alumina particles of irregular shape in the size range of $250 - 550\,\mu$m. We focused on the pre-nozzle region in which the carrier phase flow spatially accelerates towards the nozzle. We applied a two-phase, PIV/PTV algorithm and quantified the carrier and particulate phases velocity fields.

The alumina irregularly shaped particles are strongly inertial with the relatively high Stokes and particle Reynolds numbers. The particles pass the finite size flow chamber quickly, as compared to their response time scale. As a consequence, the interactions are abrupt and strong, but the residence time is much shorter as compared to the particle response time. Therefore, in this peculiar situation, the particles move at almost constant average velocity, despite the fact that the carrier phase flow rapidly accelerates towards the nozzle. This leads to the high and monotonically increasing relative (slip) velocity between the particulate phase and carrier flow.

The combination of the high particle-fluid relative velocity, slow response time and rapid acceleration of the air mean flow, leads to substantial turbulence argumentation, mostly in the streamwise component. The particle-related mechanism for these Stokes numbers range from $St > 75$ and the particle Reynolds numbers $Re_p > 300$ was termed in the literature as "vortex shedding" mechanism Hetsroni (1989); Balachndar and Eaton (2010). In the present case, in particular, the particles move slower than the carrier fluid flow. Thus, a turbulent wake is in the direction of relative velocity and effectively it is "downstream" from the particle. More detailed local flow around the particles analysis (not shown here for the sake of brevity) shows that on average a local reduction of the air flow velocity in the particle wake is pronounced up to five particle diameters downstream from the particle. We presented the comparison of the local turbulence augmentation in the proximity of the particles and compared it to the turbulence augmentation in the entire region of interest. We also demonstrated the peculiar situation of streamline convergence leading to an increase of the local mass fraction, streamwise acceleration and particle-turbulence interactions. First, the streamwise average velocity acceleration significantly reduces the streamwise turbulent fluctuations. Second, inertial particles of irregular shape create streamwise fluctuations in their wakes due to the vortex shedding and compensate the mean flow acceleration effect. In addition to the drastic increase of TKE, the particle wakes are, unexpectedly, more isotropic than the surrounding turbulence. Furthermore, particle wakes are much more isotropic as compared to the unladen flow case with the mean flow acceleration.

In our experiment, particle mass fraction is monotonically increasing towards the nozzle due to mass conservation and streamlines convergence, (see 4). Nevertheless, in the measurement region of interest the mass fraction is in the two-way coupling regime and we did not observe any clustering of particles. Our conclusions are therefore, limited to

the dilute, two-way coupling regime.

In respect to the aforementioned particle-flow dimensionless parameters, we have estimated that $P_a > 10^5$ in the entire measurement region. As suggested by Tanaka and Eaton (2008) it falls in the range that predicts an increase in turbulence. The length scales ratio, d_p/L Gore and Crowe (1989) is lower than 0.1 and predicts attenuation, however our particles lead to augmentation. This discrepancy is likely to reflect the fact that the main effect is due to the particle wakes that are five times larger than the particle effective diameter.

This empirical work does not improve significantly our ability to predict the effects of particle-turbulence interactions. However, it adds a few important observations relevant for the case of particle-laden flows with high Stokes/Reynolds numbers irregularly shaped particles, especially in the case of accelerating and converging incompressible flows. We demonstrate the mechanism, by which a small mass fraction of particles in the accelerating and converging flow leads to up to 20% increase of turbulent kinetic energy. It could lead to a comprehensive choice of the particle shape and density, (St, Re_p) and the mass fraction (number of particles per volume of solid propellant) that can compensate the decrease of TKE by the flow acceleration. Furthermore, we demonstrate that irregularly shaped particles, moving slower than the surrounding fluid, will create streamwise fluctuations that lead to the isotropic turbulence regions with important consequences for mixing and transport flux. We can infer that both the turbulent mixing and combustion rates could be enhanced using these mechanisms. The right choice of turbulence enhancing particles with the focus on the near-nozzle region shall affect the overall performance of the rocket engine and modify its exhaust content. The two-way global and local coupling mechanisms could not be neglected in numerical simulations and analytical models of multi-phase rocket engines. The presented results can serve as a benchmark for the two-phase particle-laden flow simulations in quasi-2D flows.

References

Balachndar, S., Eaton, J.K., 2010. Turbulent dispersed multiphase flow. Annu. Rev. Fluid Mech. 42, 111–133.

Caveny, L.H., Gany, A., 1979. Breakup of Al/Al_2O_3 agglomerates in accelerating flowfields. AIAA 17, 1368–1371.

Cisse, M., Homann, H., Bec, J., 2013. Slipping motion of large neutrally buoyant particles in turbulence. J. Fluid Mech. 735.

Ciucci, A., Iaccarino, G., 2012. Numerical analysis of the turbulent flow and alumina particles in solid rocket motors. J. Eng. Phys. Thermophys. 85, 1–15.

Crowe, C.T., Schwarzkopf, J.D., Sommerfeld, M., Tsuji, Y., 2011. Multiphase Flows with Droplets and Particles.

Elghobashi, S., Trusedell, G.C., 1993. On the two-way interaction between homogeneous turbulence and dispersed solid particles. I: Turbulence modification. Phys. Fluids 5, 177–216.

Elhimer, M., Praud, O., Marchal, M., Cazin, C., Bazile, R., 2017. Simultaneous PIV/PTV velocimetry technique in a turbulent particle-laden flow. J. Visual. 20, 289–304.

Gany, A., Caveny, L., Summerfield, M., 1978. Aluminized solid propellants burning in a rocket motor flow field. AIAA 16, 736–739.

Gilbert, M., Davis, L., Altman, D., 1955. Velocity lag of particles in linearly accelerated combustion gases. J. Jet Prop. 25, 26–30.

Gore, R.A., Crowe, C.T., 1989. Effect of particle size on modulating turbulent intensity. Int. J Multiph. Flow 15, 279–285.

Hardalupas, Y., Taylor, A.M.K.P., Whitelaw, J.H., 1989. Velocity and particle-flux characteristics of turbulent particle-laden jets. Proc. Royal Soc. A. 426, 31–78.

Hetsroni, G., 1989. Particles turbulence interactions. J. Multiph. Flow 15, 341–351.

Hwang, W., Eaton, J.K., 2006. Homogeneous and isotropic turbulence modulation by small heavy (St $\approx$ 50) particles. J. Fluid Mech. 564, 361–393.

Khalitov, D.A., Longmire, K., 2002. Simultaneous two-phase PIV by two-parameter phase discrimination. Exp. Fluids 32, 252–268.

Kiger, K.T., Pan, C., 2002. Suspension and turbulence modification effects of solid particulates on a horizontal turbulent channel flow. J. Turb. 3, 1–21.

Kulick, J.D., Fessler, J.R., Eaton, J.K., 1994. Particle response and turbulent modification in fully developed channel flow. J. Fluid Mech. 277, 109–134.

Kussin, J., Sommerfeld, M., 2002. Experimental studies on particle behaviour and turbulence modification in horizontal channel flow with different wall roughness. Exp. Fluids 33, 143–159.

Li, J., Wang, H., Li, Z., Chen, S., Zheng, C., 2012. An experimental study on turbulence modificion in near-wall boundary layer of dilure gas-particle channel flow. Exp. Fulids 53, 1385– 1403.

Meller, Y., Liberzon, A., 2015. Particlefluid interaction forces as the source of acceleration PDF invariance in particle size. Int. J. Multiph. Flow 76, 22 – 31.

Poelma, C., Westerweel, J., Ooms, G., 2006. Turbulence statistic from optical whole-field measurements in particle-laden turbulence. Exp. Fluids 40, 347–363.

Prevost, F., Boree, J., Nuglisch, H.J., Charnay, G., 1996. Measurements of fluid/particle correlated motion in the far field of an axisymmetric jet. Int. J. Multiph. Flow 22, 685–701.

Riley, N.A., 1941. Projection sphericity. J. Sediment. Petrology 11, 94–97.

Tanaka, T., Eaton, J.K., 2008. Classification of turbulence modification by dispersed spheres using novel dimensionless number. Phys. Rev. Lett. 101, 297– 285.

Volkov, K.N., Emel'yanov, V.N., Kurovs, I.V., 2012. Flow and motion of condensed-phase particles in the prenozzle space on solid-propellant rocket motors. J. Eng. Phys. Thermophys. 85, 724–731.

Wadell, H., 1935. Volume, shape and roundness of rock particles. J. Geology 40, 443–451.